Lamella-rod pattern transition and confinement effects during eutectic growth

Melis Şerefoğlu, Sabine Bottin-Rousseau, Silvère Akamatsu

Lamella-rod pattern transition and confinement effects during eutectic growth

Melis Şerefoğlu[a,b], Sabine Bottin-Rousseau[a], Silvère Akamatsu[a]

[a] *Sorbonne Université, CNRS-UMR 7588, Institut des NanoSciences de Paris, case courrier 840, 4 place Jussieu, 75252 Paris Cedex 05, France*

[b] *Department of Metallurgical and Materials Engineering, Marmara University, Maltepe, İstanbul, Turkey*

Abstract

We present an in situ experimental study of rod-like and lamellar growth patterns during directional solidification of a model eutectic transparent alloy, namely the succinonitrile-(d)camphor (SCN-DC) system. Coupled-growth patterns, and their morphological transformations upon changes of the pulling velocity V ($0.0035 - 0.07$ μms^{-1}), were observed in real time in a series of flat-wall samples with different thicknesses δ from 15 (thin samples) to 350 μm (thick samples). While rod-like patterns formed systematically at relatively large velocity, both lamellae and rods were observed at sufficiently low velocity, regardless of the sample thickness. In confined-geometry samples ($\delta = 30 - 140$ μm), lamellar patterns were stabilized over a large range of the interphase spacing λ at low V. In this thickness range, the lamella ends in contact with the sample walls were stabilized, and lamellar breakup into rods was mediated by secondary instabilities such as a zigzag mode and a spatial-oscillation mode. The (reverse) transition from rods to lamellae involved both rod elimination and rod elongation instabilities. In the bistable range, a hysteresis upon increasing or decreasing V was observed, as well as complex phenomena involving oscillatory, mixed and hybrid patterns. A discussion on the elementary mechanisms that determine the lamellar-rod transition, and their dependence on λ and V is initiated.

Keywords: A1.Directional solidification, A1.Eutectics, A1.Morphological stability

1. Introduction

Composite solidification microstructures in nonfaceted binary eutectic alloys are a frozen trace of a coupled, diffusion controlled growth of two different crystal phases [1, 2, 3]. The self-organizing dynamics of coupled-growth patterns at the propagating solid-liquid interface, and hence the shape of the two-phase microstructures in the bulk solid, depend on alloy characteristics and control parameters [4, 5]. They also are sensitive to boundary and initial conditions [6, 7]. During directional solidification at an imposed velocity V in a fixed temperature gradient, planar coupled-growth patterns can form in steady-state. They basically exhibit periodic, hexagonal or banded arrangements that result in bulk eutectic growth microstructures with rod-like or lamellar shapes in the solid, respectively. The interphase (inter-rod or inter-lamellar) spacing λ

Email address: akamatsu@insp.jussieu.fr (Silvère Akamatsu)

ordinarily falls close to a scaling length λ_m, which is determined by chemical diffusion in the liquid and capillary effects. The characteristic spacing λ_m approximately varies with V as $V^{-1/2}$ [5]. At given V, however, rod-like and lamellar eutectic patterns exhibit spacing values that can vary within finite intervals, and depend on the history of the solidification process. Outside their stability intervals, rod-like and lamellar patterns undergo morphological instabilities [7, 8], which arise through the amplification of symmetry breaking (e.g., oscillatory, drifting, or zigzag) modes [9, 10]. The threshold spacing of those symmetry-breaking (or secondary) instabilities, which delimit the stability intervals, are approximately proportional to λ_m [11, 12, 13, 14, 15, 16]. According to numerical simulations, the rod and lamella stability intervals overlap over a finite range of λ and V values, leaving open the possibility of a dynamic metastability of lamellar and rod-like patterns [17]. However, while secondary instabilities do not change the basic topology of the coupled-growth patterns [9, 10], the shape transformation from lamellae to rods, and the reverse one, involve the disruption, or breakup, of the triple-junction lines (trijunctions) at which the two solids and the liquid are in contact. The lamella-rod transition is thus a discontinuous process, and gives rise to highly nonlinear, particularly complex spatio-temporal phenomena [8, 17, 18, 19, 20, 21, 22, 23, 24, 25]. Among key results, the lamellar breakup was shown to result from the amplification of a propagative instability that resembles a Rayleigh-Plateau instability [17, 22, 26]. Recently, it has been revealed experimentally that lamellar and rod-like patterns can coexist spatially in the form of large domains [22]. Intriguingly, long lamellae were observed at a very low pulling velocity only, whereas at higher V values, rod-like patterns systematically formed. This raises important, yet incompletely addressed questions relative to precursory instability modes, the dynamic metastability of lamellar and rod-like patterns, the relevance of the $V^{-1/2}$ scaling law, the formation of hybrid or domain-like microstructures, and a possible microstructure selection process.

In this paper, we present an experimental study of the dynamics of eutectic growth microstructures in confined-geometry conditions, using a directional-solidification setup that permits real-time observation of the coupled-growth front with a top-view optics in transparent alloys [27]. The model system chosen, the nonfaceted succinonitrile-(d)camphor (SCN-DC) eutectic alloy [28], is known to ordinarily form rod-like microstructures –with rods of the DC solid phase dispersed in a continuous SCN solid matrix [29, 30, 31]. The rod-like microstructure is favored by a relatively low value of the volume phase fraction η of the DC phase in the solid ($\eta \approx 0.24$). The SCN-DC system also presents the advantage, in the present context, that most eutectic grains can be considered as essentially isotropic (for a study of the effect of a strong interfacial anisotropy on the lamella-rod transition, see, e.g., Ref. [32]). Here, directional solidification experiments were carried out using a series of flat, glass-wall samples with various values of the thickness δ between 15 (thin samples) and 350 μm (thick samples). In practice, a thin sample is considered as being equivalent to a two-dimensional (2D) system [7, 33, 34], while a thick sample is representative of a bulk, three-dimensional (3D) system [30, 31]. Confined-geometry, or confinement effects are expected to occur in samples with intermediate thicknesses. To illustrate the problem, a regular rod-like microstructure in a 400-μm thick sample, and a lamellar pattern in a much thinner sample are shown in Figs. 1a and 1b, respectively. The phenomenology of confinement effects in out-of-equilibrium pattern forming systems has been an important topic in nonlinear physics [9]. The problem has also been more specifically addressed during directional solidification of dilute alloys, and a transition from fully 2D to 3D deep-cell growth patterns, via confined shapes, was demonstrated [35]. In the case of directionally solidified eutectics, it was commonly assumed that a 3D- to 2D-growth transition could occur for sample thicknesses decreasing down to values below, or on the order of the interphase spacing (i.e., $\delta \leq \lambda$). The present observations

of confined eutectic growth patterns revealed a higher level of complexity, and studying them was particularly instructive.

We took advantage of real-time observations of the evolution of coupled-growth patterns over the whole thickness of the samples during directional-solidification experiments. The use of a confined geometry made it possible to form steady-state growth patterns at fixed pulling velocity, and to follow transient regimes subsequent to upward or downward velocity changes (velocity jumps), starting from a well-defined, nearly uniform initial state. By this way, elementary morphological instabilities were identified. Our main purposes were (i) to map out the steady-state morphologies in a parameter space including the sample thickness δ, the growth velocity V, and the spacing λ, (ii) to investigate the transition mechanisms between different morphologies, aiming at identifying the instability modes at play, and (iii) to examine the (relative) stability of different types of coupled-growth patterns, including periodic patterns involving elongated rods and hybrid motives have also been found numerically [17, 21], in addition to the standard rod-like and lamellar patterns.

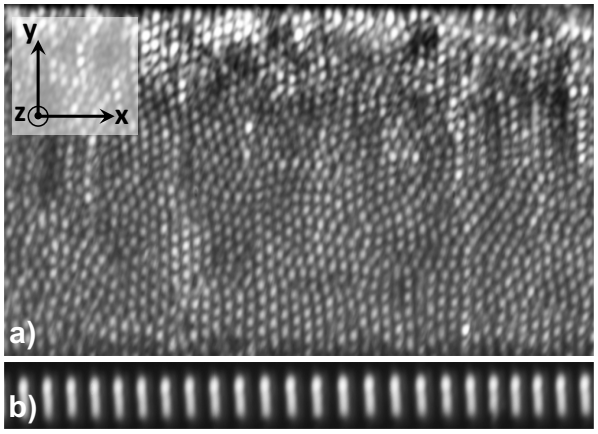

Figure 1: Coupled-growth patterns observed in real time during directional solidification of a eutectic SCN-DC alloys in two samples of different thicknesses δ. In the top-view imaging method that is used in this paper, DC-liquid interfaces appear as bright disks or bands, while the SCN-liquid interfaces are dark. Horizontal dimension of the panels: 650 μm. The samples were of a much larger extension in the lateral direction **x**. The main solidification axis **z** points toward the reader. a) Rod-like pattern in a 400-μm thick sample; $V = 0.0525\ \mu\text{ms}^{-1} (= 15V_0)$. The vertical dimension of the image was adjusted to fit the thickness of the sample in the transverse direction **y**. b) Lamellar pattern in a 60-μm thick sample; $V = 0.0105\ \mu\text{ms}^{-1} (= 3V_0)$. The lamellae terminate in contact with the glass walls. See section 2 for technical details.

A list of parameters is given in Table A1 (see Appendix A below). For the sake of clarity, the abbreviations 2D and 3D will be used for two- and three-dimensional dynamical phenomena in thin and bulk samples, respectively. The terms 1D- and 2D-(periodic) patterns will designate coupled-growth patterns with a periodicity in one direction and two directions, respectively. In practice, 1D (lamellar) patterns can be observed in both 2D and 3D systems, while 2D (rod-like) patterns exist in 3D and confined systems only. Experimental methods will be presented in section 2. The main results of this study will be reported in section 3. A discussion is proposed in section 4, and conclusions and prospects are presented in section 5.

2. Experimental methods

The nonfaceted transparent SCN-DC eutectic alloy (eutectic temperature $T_E = 37.1 \pm 0.5$ °C; concentration of the eutectic liquid $C_E = 13.5 \pm 0.3$ mol%) solidifies into nearly pure SCN and DC solid phases [28]. It has been previously used for several in situ solidification studies [20, 29, 30, 31]. At the eutectic concentration, the phase fraction of the DC solid phase η is of about 0.24. The characteristic constant $\lambda_m^2 V$ [5] has been previously estimated to a value of 10.2 ± 1.5 μm^{3}s^{-1} [29]. Commercial SCN and DC were purified by double distillation and sublimation, respectively. A eutectic alloy was prepared by weighting and mixing purified SCN and DC in the liquid state under low-pressure Argon atmosphere. For solidification experiments, rectangular containers made of two (0.3-mm thick) flat glass plates separated by PET spacers, which determine the thickness of the sample, were used. Six values –15, 30, 60, 100, 140 and 350 μm (± 3 μm)– of the actual thickness δ of the sample were used for systematic investigation of the confinement effect. The other dimensions of the samples were typically of 60 mm along the growth direction **z**, and 6 mm along **x**. In order to grow eutectic grains with no apparent crystal anisotropy, the PET spacers were designed with a funnel-like shape (thin crystal selector channel, V-shaped crystal expander) on one end of the sample (placed at the cold part of the solidification setup [36]). Sample filling was made by capillarity in the liquid state under protective Argon atmosphere, followed by rapid cooling down to room temperature, and sealing.

In the directional-solidification bench [27], the value of the temperature gradient G (along axis **z**) was 8 ± 1 Kmm^{-1}. For solidification, the displacement (or pulling) of the samples along the temperature gradient axis **z** was ensured by a DC motor (PI). Pulling velocities down to the set minimum value ($V_0 = 0.0035$ μms^{-1}), and entire multiples of V_0 (e.g., $2V_0 = 0.007$ μms^{-1}, $3V_0 = 0.0105$ μms^{-1}, and so on) were used. The term "high" velocity will be conveniently used for larger V values up to $20V_0 = 0.07$ μms^{-1}. In steady-state, the solidification rate is equal to V. Within the $V_0 - 20V_0$ interval, λ_m was falling between 12 and 54 μm, which, in practice, permitted to record well contrasted images of good optical quality.

The optical setup permits to capture top-view images of the whole solidification front in real time [27, 36]. Dark-field, transmitted-light images are obtained with a long-distance microscope focussing the solid-liquid interface in oblique view, from the exterior of the sample, through the liquid and the glass walls. The DC crystals in contact with the liquid appear white, in strong contrast with the SCN matrix. A small-aperture diaphragm is used for selecting the light coming out of one solid phase (here, DC) only. The actual optical resolution was of about 3 μm. Raw oblique-view images are contracted in the vertical direction. They were rescaled numerically to a 1:1 aspect ratio by a factor 2.5 in the direction **y** (for a viewing angle of 48^o) [27]. The field of view of individual images, recorded on a PC computer via a numeric camera, was typically 300 to 700 μm in the lateral direction **x**. The entire microstructure of the solid-liquid interface was visible, and well focused, in the transverse direction **y**, for all the values of the sample thickness used in this study. Some global-filtering procedures (background subtraction, gaussian smoothing, contrast enhancement) were used for both display and analysis purposes.

The experiments were carried out as follows. A sample was submitted to rapid (and partial) directional melting in the apparatus. Directional solidification was then started at a high velocity (typically $20V_0$) from the remaining solid seeds in the crystal-selector channel up to the end of the V-shaped crystal expander. At that stage, a few eutectic grains of large size were present. The pulling velocity was then slowed down, and solidification continued until a steady-state pattern formed. Solidification at constant V was run over times ranging typically between 8 to 100 hours. Sudden morphological changes just after velocity jumps, and smoother rearrangements

occurring over longer timescales were monitored continually.

Let us finally note that the directional-solidification study of Ref. [22] was carried out in microgravity to avoid thermosolutal convection in the liquid. In that work, a eutectic SCN-DC alloy was enclosed in a large, 1-mm thick sample. The present study was carried out on ground in a regular research laboratory with thinner samples; no detrimental fluid motion was observed.

3. Results

3.1. Thin samples

In thin eutectic SCN-DC samples, 1D-periodic coupled-growth patterns can form over a wide λ range. This is illustrated in Fig. 2 –the images have been captured in the same top-view mode as that used for thick samples, instead of the side-view imaging that is more usual for thin samples (see supplemental material [36]). A small-spacing pattern at relatively high velocity ($V = 10V_0$) is shown in Fig. 2a. In that image, the average spacing $\lambda_{av} = 17.2\ \mu$m, was nearly equal to λ_m at that velocity –and very close to the sample thickness $\delta = 15\ \mu$m. The patterns shown in Fig. 2b and Fig. 2c were both observed at a much lower velocity ($V = 2V_0$). In Fig. 2b, we measured $\lambda_{av} = 33\ \mu\text{m} = 0.90\lambda_m$, which also falls in the stable range for bulk samples. In Fig. 2c, the average spacing $\lambda_{av} = 78\ \mu\text{m} = 2.1\lambda_m$ reached such a large value that the coupled-growth pattern was actually in an oscillatory regime [36]. Such time oscillations ("1λO" mode [7]) are typically observed in 1D-patterns with spacing values in the $2\lambda_m$ range [13, 14, 29]. They are practically inaccessible in bulk samples, being well above the rod or lamellar splitting limits. Let us also note for clarity that, in spite of a misleading appellation, 1λO oscillations in 1D patterns must not be mistaken for the spatial 1λ oscillation mode, which is generic to lamellar patterns in 3D systems, and will also be mentioned later on in this paper.

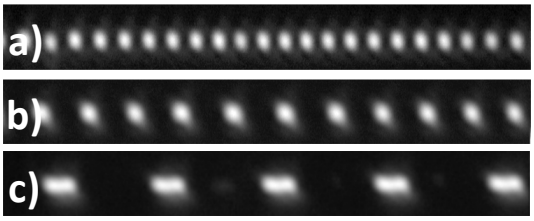

Figure 2: Directional-solidification patterns of a eutectic SCN-DC alloy in a thin sample ($\delta = 15\ \mu$m). a) $V = 10V_0 = 0.035\ \mu\text{ms}^{-1}$. b) and c) $V = 2V_0 = 0.007\ \mu\text{ms}^{-1}$. Horizontal dimension: 360 μm.

3.2. Coupled-growth patterns in confined-geometry samples

A regular rod-like pattern in a thick SCN-DC sample of eutectic concentration is shown in Fig. 1a. It can be seen, in brief, that, on a local scale, the rod-like pattern basically arranged into hexagons [17], and that, on a larger scale, it was made of small hexagon domains separated by topological defects [36, 37, 38]. As a contrasting example, Fig. 1b shows a 1D-periodic pattern in a confined geometry with a lamellar spacing (27.1 μm on average) that is substantially smaller than the sample thickness $\delta = 60\ \mu$m. As mentioned above, this new, and central observation brings clear evidence that the common-wisdom $\delta \leq \lambda$ criterion for the stability of 1D-periodic

patterns is failing. In this section, additional, and more detailed observations are presented along with new information on the lamella-rod transition extracted from them.

Representative images of coupled-growth patterns observed in eutectic SCN-DC samples of different thicknesses at constant pulling velocity are shown in Fig. 3. In confined samples, both rod-like and lamellar patterns were observed, depending on the velocity.

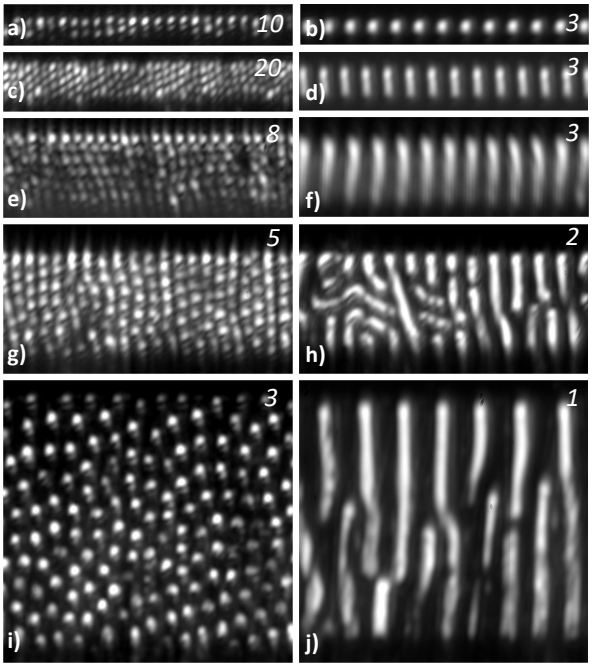

Figure 3: Rod-like (left column) and lamellar (right column) patterns in eutectic SCN-DC samples of various thicknesses. From top to bottom, $\delta = 30, 60, 100, 140$, and $350\ \mu$m. Pulling velocities are indicated in terms of V/V_0, with $V_0 = 0.0035\ \mu\text{ms}^{-1}$ (top right corner of each panel). d) Same sample as in Fig. 1b. Horizontal dimension: $370\ \mu$m [a) to f)]; $410\ \mu$m [g) to j)].

Rod-like patterns at relatively large V values in samples of increasing thickness (from top to bottom) are shown in the lefthand panels of Fig. 3. As in bulk samples, hexagonal patterns were observed on a local scale, and the average spacing was close to λ_m. More details can be added. The persistent disorder in the thicker sample (Fig. 3i) is characteristic of rod-like patterns at very low pulling velocity [31]. Oscillatory behaviors were observed in samples with intermediate thicknesses (see section 3.5). An instrumental effect, namely, the influence of a mild, large-scale curvature of the isotherms in the transverse direction, has been detected in the experiments –this has been carefully analyzed in a previous study [30]. In brief, the envelope of the solidification front slightly bulges into the liquid on a centimeter scale, due to a difference of thermal conductivity of the different media in presence. This entails a slow stretching of the pattern along the **y** direction, and the elimination of rods at the sample walls. The average value λ_{av} of the inter-rod spacing continually increases, until it approximately reaches the rod-splitting limit λ_{sp}. Over long solidification times, the stretching effect is counterbalanced by frequent rod splittings, and the system reaches a quasi steady-state regime. The curvature effect also entails a

progressive alignment of the hexagon structure. This can be seen in Figs. 1a, and 3g.

The central result of the study is the formation of lamellar patterns (righthand panels of Fig. 3) in both thin (Fig. 2), confined (Figs. 3b, 3d, 3f, 3h) and thick samples (Fig. 3j), at very low pulling velocity (typically $V \leq 3V_0$). Remarkably, steady-state 1D patterns with straight lamellae connecting the two opposite walls of the sample were observed for δ values less than, or equal to 100 μm. For larger thicknesses (Fig. 3h for $\delta = 140$ μm, and Fig. 3j for $\delta = 350$ μm), more disordered patterns persistently formed, in spite of long pulling times. Those coupled-growth microstructures are actually similar to labyrinth patterns that are of common occurrence in extended, isotropic systems [15, 16, 39, 40]. Let us note that the pattern of Fig. 3j was observed at $V = V_0$, hence at a velocity that was half of the smallest V value achieved in Ref. [22].

Quantitative measurements are presented in the graphs of Fig. 4. Different symbols are used to distinguish between the following groups of measurement data points. Filled disks correspond to rod-like patterns, and large square symbols to lamellar patterns. Smaller square symbols correspond to 1D patterns in thin samples. Other symbols correspond to more complex –oscillatory (white disks) and mixed (diamonds)– patterns. The V-δ graph of Fig. 4a can be seen as a list of the different solidification runs. As stated above, rod-like patterns are favored by large V values, and lamellar patterns by small V values. One can define a limit velocity V_r above which no lamellar patterns were observed, and, more surprisingly, another limit V_l below which no rod-like patterns were observed. The $V_l < V < V_r$ velocity range is defined as the bistable domain, within which rod-like, lamellar and mixed patterns can be observed. Roughly speaking, V_l is estimated to fall between V_0 and $2V_0$, and V_r between $3V_0$ and $4V_0$. The quantities V_l and V_r do not seem to vary much with the sample thickness, except that V_r increases substantially for δ below 60 μm. The latter feature simply indicates that, in thinner samples, hexagon patterns can only form in steady-state for small values of the interphase spacings, within a λ range that is accessible at higher velocities, according the approximate λ_m scaling. In very thick samples (Figs. 3i and 3j), lamellar (or labyrinth) patterns were solely observed for $V = V_0$. At that velocity, no 2D rod-like patterns were observed, and lamellar patterns were systematically obtained regardless of the value of the sample thickness.

We measured the interphase spacing (averaged over a few repeat units) in representative images of relatively well ordered patterns or domains. In the λ-δ graph of Fig. 4b, it appears clearly that lamellae are favored by large spacings, and rod-like patterns by small spacings. Let us define λ_l as being the spacing value below which no steady-state lamellar (or labyrinth) patterns were observed. One can see that λ_l remained essentially constant (28 ± 1 μm) in confined-geometry samples. It is worth noting again that, for $\delta = 60, 100$ and 140 μm, lamellar pattern were observed for λ values well below the sample thickness ($\lambda_l < \delta$). For $\delta = 350$ μm, λ_l increased substantially (to about 40 μm). The respective domains of existence of rod-like and lamellar patterns actually overlap with each other for an intermediate λ range –within which oscillatory, mixed and hybrid patterns were observed as well.

Finally, we reported λ as a function of V in Fig. 4c –thus eliminating δ as a parameter. As previously observed in the SCN-DC system [29, 31], the spacing distribution roughly followed the same $V^{-1/2}$ scaling as λ_m. It was relatively wide, in particular at low velocity. More interestingly, it again appears clearly that rod-like patterns are favored by small λ and large V values, and lamellar patterns by large λ and small V values –with a finite overlap. In Fig. 4d, the same measurement data as those of Fig. 4c are represented in a $\Lambda = \lambda/\lambda_m$-$vs$-$V$ diagram. As concerns the relative stability of rods and lamellae, no specific scaling is revealed in this graph. For the sake of completeness, we plotted the rod splitting threshold λ_{sp} and the rod elimination threshold

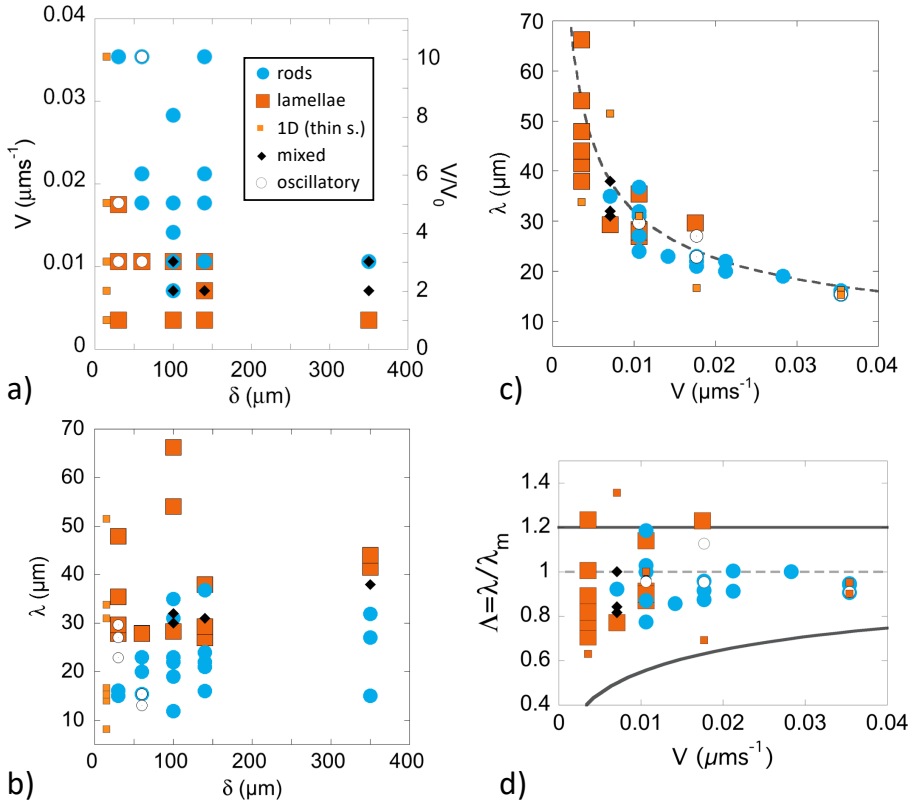

Figure 4: Morphology maps of coupled-growth patterns in the eutectic SCN-DC system. a) Pulling velocity V vs. sample thickness δ ($V_0 = 0.0035\ \mu\text{ms}^{-1}$). b) Interphase spacing λ vs. sample thickness δ. c) Interphase spacing λ vs. pulling velocity V (dashed line: λ_m). d) Dimensionless interphase spacing $\Lambda = \lambda/\lambda_m$ vs. velocity V; same data as in Fig. 4c (horizontal dashed line: $\Lambda = 1$); for the rod splitting threshold $\lambda_{sp}/\lambda_m \approx 1.2$ (continuous, horizontal line) and the rod elimination threshold λ_{el}/λ_m (bottom line), see Ref. [31]. Large (small) squares: lamellar patterns (1D patterns in thin samples). Filled disks: rod-like patterns. Diamonds: mixed patterns. White disks: oscillatory patterns. For a clear view of the data points of interest, the V axes were intentionally limited to values below $11V_0$ in a), c), and d), and the λ axes between 10 and 70 μm in b) and c).

λ_{el}. As established in Ref. [31], it is known that $\lambda_{sp} \approx 1.2\lambda_m$, and that λ_{el} is smaller than λ_m, and depends on the ratio G/V (overstability phenomenon) [41]. The measurement data of the present study corresponding to rod-like patterns fall well inside the relevant stability domain. Lamellar spacing measurements in the SCN-DC system are the first of their kind, to the best of our knowledge (except for a few ones reported in Ref. [22]). They fall within the same range as that of rod-like patterns, which seems a necessary condition for making a bistable behavior possible. This will be discussed further in section 4 below.

3.3. Mixed patterns - Hysteresis

Not only steady-state lamellar and rod-like patterns, but also complex, "mixed" patterns were observed for intermediate values of the parameters. Illustrative examples are shown in Fig. 5. The two images were captured in the same 350-μm thick sample as in Figs. 3i and 3j. In Fig. 5a, one can see an essentially rod-like pattern with short lamellae and dumbbell- (or peanut-)like rods [17, 21] in the core of the pattern, observed at $V = 3V_0$, that is, in the same conditions as Fig. 3i. The lamellae were unstable. Their length remained limited to a few times the value of the spacing in the surrounding pattern, and did not increase further due to a breakup instability at their free ends (also see Ref. [22]). The short lamellae also aligned more or less parallel to the transverse direction **y**, under the same large-scale curvature effect as mentioned above. The mixed coupled-growth pattern of Fig. 5b was observed at a lower velocity ($V = 2V_0$) than that of Fig. 5a –but higher than the lamellar pattern of Fig. 3j. It was mostly lamellar, with isolated rods. Therefore, as the velocity was decreased, the length and the fraction of lamellae increased in the mixed pattern, while rods became less numerous. Such mixed patterns are reminiscent of previous ex situ observations in directionally solidified Al-Al_2Cu eutectic samples [18]. As shown in Fig. 3j, at even lower velocity, rod-like patches disappeared, and a fully lamellar pattern was left growing.

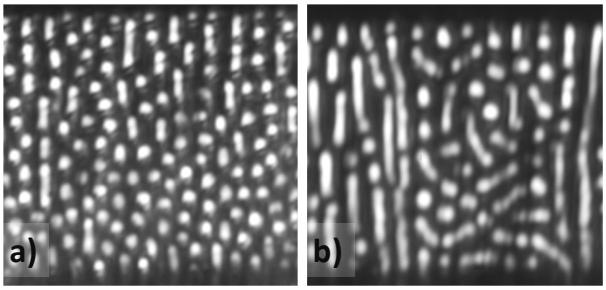

Figure 5: Mixed lamellar-rod solidification patterns in a $\delta = 350\ \mu$m SCN-DC sample. a) $V = 3V_0 = 0.0105\ \mu\text{ms}^{-1}$. b) $V = 2V_0 = 0.007\ \mu\text{ms}^{-1}$. Horizontal dimension: 410 μm.

The above observations (in brief, the overlap of stable rod-like and lamellar domains in the graphs of Fig. 4, and the formation of mixed patterns) indicate a dynamic metastability of rod-like and lamellar patterns over a finite, intermediate range of V and λ values (bistable domain). This property was more clearly revealed during an experiment aiming at evidencing the history dependence of the system [25]. The rod-like pattern of Fig. 6a was observed at $V = 3V_0$ after a downward velocity jump. The initial condition was a rod-like pattern with a smaller spacing obtained at $V = 10V_0$. A standard rod-elimination process lead to the structure of Fig. 6a. The

lamellar pattern of Fig. 6b was observed at the same velocity (and in the same sample) as Fig. 6a, but after an upward velocity jump. Into more details, the pulling velocity had been previously set to $V = V_0$, and the lamellar pattern obtained at that velocity served as a new initial condition [25] –also see the section 3.4. In other words, a rod-like pattern and a lamellar pattern were observed in the very same sample, at the very same velocity, after two opposite experimental paths were imposed on the system. As in Fig. 5, the resulting two patterns were not fully uniform (short lamellae within rods in Fig. 6a, and rod-like patches surrounded by lamellae in Fig. 6b). The average spacing in the rod-like pattern of Fig. 6a ($\lambda = 0.71\lambda_m$) was smaller than that in the lamellar pattern of Fig. 6b ($\lambda = 0.85\lambda_m$). In other words, at given V, the stability domain of lamellae extends up to larger spacing values than that of rod-like structures.

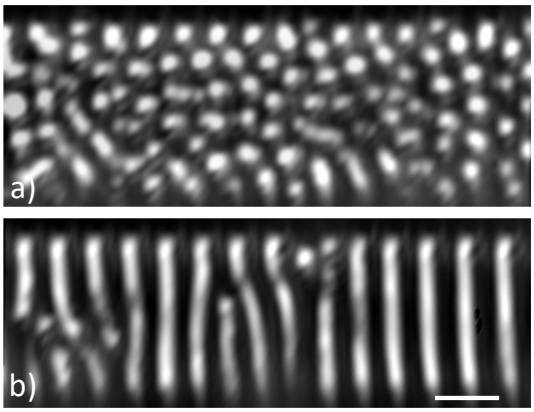

Figure 6: Rod-like (a) and lamellar (b) eutectic growth patterns in a $\delta = 140\ \mu$m SCN-DC sample. The two patterns were observed in the same sample, at the same velocity ($V = 3V_0 = 0.0105\ \mu\text{ms}^{-1}$), after a downward velocity jump in a), and an upward velocity jump in b). Bar: 50 μm.

3.4. Morphological instabilities during transients

Transient spatio-temporal processes leading to a lamella-rod transition could be followed in confined-geometry samples starting from a well-defined initial condition. The experimental protocol, of common practice during in situ solidification experiments, consisted in the formation of a (nearly) periodic, steady-state pattern at fixed V, followed by a velocity jump –upward or downward–, for testing the stability of a lamellar or a rod-like pattern, respectively. In a first experiment (Fig. 7), a 1D-periodic lamellar pattern was formed at $V = 3V_0$ in a $\delta = 60\ \mu$m sample. The pattern exhibited a spatial modulation of the spacing (average spacing $\lambda_{av} \approx 29.5\ \mu$m) on the scale of the field of view [36]. At time $t = 0$, the velocity was doubled to $V = 6V_0$. After a maturation time (≈ 2 hours), the lamellar pattern became unstable, and the transformation to rods took place. Three stages could be distinguished. First, a morphological instability started at the spot where the spacing was at its maximum, and propagated in the two opposite directions along **x** (first stage; blue frame in Fig. 7). The incipient spatial undulation of the lamellae was similar to a zigzag mode that has been identified previously in 3D samples of the lamellar transparent eutectic alloy CBr_4-C_2Cl_6 [15, 16]. We recall that, on the large-λ side, the zigzag instability –above a threshold spacing λ_{zz} close to λ_m– generically transforms straight lamellae into "chevron" patterns [36]. During the second stage (red frame in Fig. 7), the shape of the lamellae progressively

became more and more distorted, ending up with a propagating lamellar-to-rod transition, each lamella typically splitting into three rods. The small-scale details of the morphological change were only partly resolved optically. At the end of that stage, the coupled-growth pattern was made of a rod-like domain (on the right), and a transient lamellar domain (on the left). During a long intermediate period of time, no additional lamellar breakup occurred in the field of view, but the spacing distribution evolved, with a slow decrease of the local spacing in the lamellar domain down to a value (22.6 μm). During the last stage (green frame in Fig. 7), the small-spacing lamellae broke up directly into rods. In that case, the instability occurred uniformly along each lamella, without any transient zigzaging shape, to within the optical resolution. That process was propagative as well. The whole coupled-growth pattern eventually exhibited a fully rod-like morphology –see section 4 for additional comments.

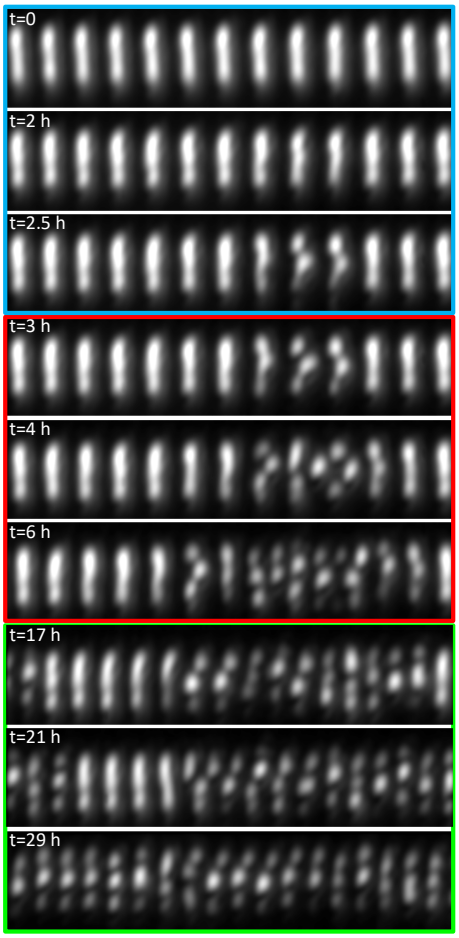

Figure 7: Series (time sequence) of images showing a lamellar-to-rod transition during directional solidification of eutectic SCN-DC in a $\delta = 60$ μm sample, after an upward velocity jump (time $t = 0$) from 0.0105 ($3V_0$) to 0.021 μms^{-1} ($6V_0$). Blue, red and green frames: incipient, zigzag-like instability, lamellar-breakup instability in the large-spacing region, and lamellar-breakup instability in the small-spacing region, respectively (color online). Time (see top left corners) runs from top to bottom. Time intervals are not constant. Horizontal dimension: 410 μm.

The reverse process, that is, a rod-to-lamellar transition is shown in Fig. 8. Starting from the rod-like pattern formed at the end of the above experiment (Fig. 7), the velocity was changed from $V = 6V_0$ back to $3V_0$ at (new) time $t = 0$. First, as expected, some rods were eliminated, and the spacing increased. Then the pattern became unstable against the elongation of some of the rods, which eventually formed stable lamellae connecting the two samples walls. The remaining rods were eliminated. The merging (or coalescence) of neighboring rods did not occur, as far as we can tell considering the limits of the optical resolution. The transformation was not fully completed before the experiment was interrupted, and a few rods subsisted. In overall, however, the final 1D pattern was quite similar to that shown in the top panel of Fig. 7.

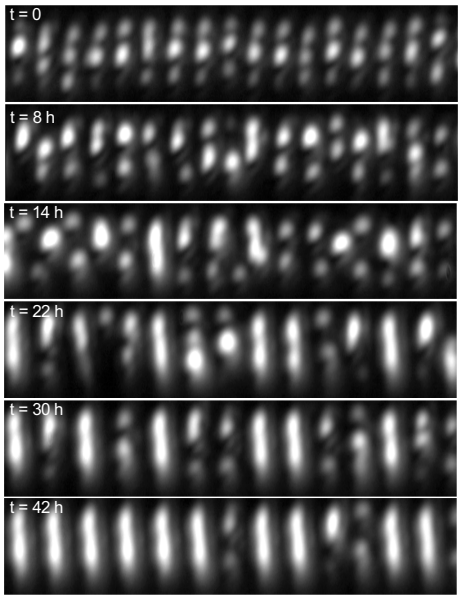

Figure 8: Rod-to-lamellar transition after a downward velocity jump from 0.021 ($6V_0$) to 0.0105 μms^{-1} ($3V_0$). Same ($\delta = 60\ \mu$m) eutectic SCN-DC sample as in Fig. 7. Horizontal dimension: 410 μm.

Finally, Fig. 9 shows a (detail of a) transient coupled-growth dynamics observed in a $\delta = 100\ \mu$m sample after an upward velocity jump. The initial microstructure (first panel of Fig. 9) was a steady-state 1D pattern at $V = V_0$ ($\lambda_{av} = 62\ \mu\text{m} = 1.15\lambda_m$). After the velocity has been increased to $3V_0$, a zigzag-like instability, and then a lamellar breakup process occurred, in a way similar to the first two stages of Fig. 7. However, after a complex spatio-temporal rearrangement involving rod elongation and rod elimination, stable lamellae formed again, and a fully 1D pattern with a smaller lamellar spacing invaded the growth front ($\lambda_{av} = 30\ \mu\text{m} = 0.95\lambda_m$). In other words, in the SCN-DC alloy, the decrease of the average spacing in a lamellar pattern, as it can be expected subsequent to an increase of the solidification velocity, occurs as a lamellar-rod-lamellar process. It is qualitatively different from the branching process that has been evidenced in bulk samples of the basically lamellar Al-Al_2Cu eutectic alloy (see Fig. 8 of Ref. [39]). The present observation brings additional evidence for the existence of lamellar patterns, and their stability in a confined geometry, over a finite range of (low) V values in the SCN-DC system.

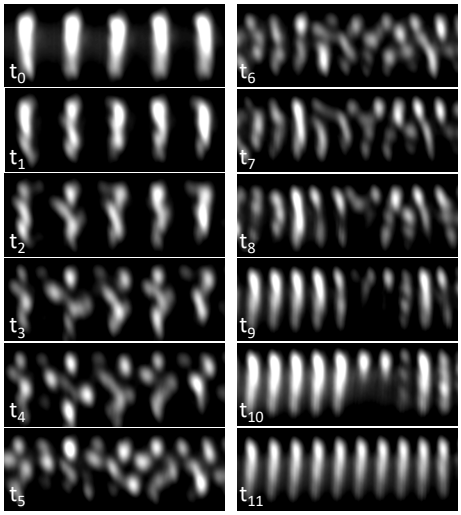

Figure 9: Lamellar-rod-lamellar transient dynamics after a velocity jump from $V_0 = 0.0035\ \mu\text{ms}^{-1}$ to $3V_0 = 0.0105\ \mu\text{ms}^{-1}$ in a $\delta = 100\ \mu$m SCN-DC sample. Time step $t_{i+1} - t_i$ between two subsequent images: 261 mins. Horizontal dimension of each panel: 290 μm.

3.5. Oscillatory and hybrid patterns

Periodic oscillations are frequent in 1D patterns during directional solidification of thin eutectic samples [29]. Oscillatory behaviors have also been reported in rod-like patterns in thick samples [31]. In the present study, time oscillations in samples of intermediate thicknesses were associated with an alternation of rod eliminations close to the sample walls, and rod splittings. In the example of Fig. 10a, a complex elimination/splitting dynamics occurred within columns of rods perpendicular to the sample walls. In that particular case, elimination/splitting cycles occurred repeatedly in opposition of phase between nearest-neighbor columns. This operating mode more or less preserved a short-range hexagonal stacking. In this experiment, and in most rod-like patterns in confined-geometry samples, oscillatory behaviors were influenced by the stretching effect induced by the curvature of the solidification front. It may be interesting to note as well that, in confined samples, oscillations can also originate from a geometric "frustration" that is expected in situations, frequent in the experiments (see Fig. 3a), where δ is not an entire multiple of a stable λ value.

Hybrid microstructures were also observed. That term designates here an essentially periodic pattern with a complex motif made of lamellae and rods. One of them, made of a spatial, 1D alternation of rods and (short) lamellae, has been observed over long experimental times in samples of different thicknesses (Fig. 10b, top and middle panels). The spatial period in the **x** direction is doubled as compared to a basic lamellar pattern. This pattern is qualitatively similar to the numerical simulation shown in Fig. 6 of Ref. [17]. Nearly similar –localized– morphologies could be observed during transient processes in thicker samples (Fig. 10b, bottom panel).

4. Discussion

The present study establishes the existence of a bistable domain in the λ-V parameter space within which both rod-like and lamellar patterns can be observed experimentally during cou-

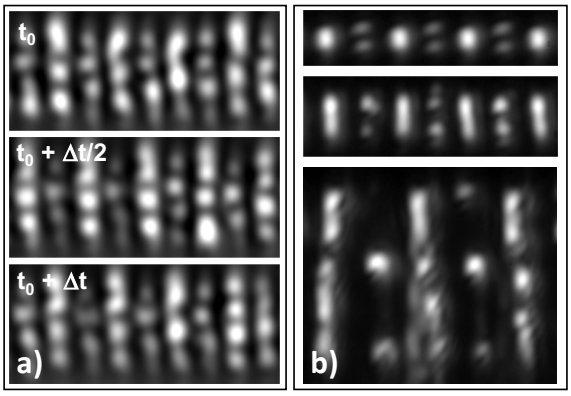

Figure 10: a) Oscillatory dynamics in a 60-μm thick SCN-DC sample. The top (time t_0) and bottom (time $t_0 + \Delta t$) images are essentially identical, with one out of two columns of rods appearing brighter. In the middle image (time $t_0 + \Delta t/2$), the same alternation is shifted laterally by one columns. Δt = 106 mins: approximate time period of the oscillation. $V = 5V_0 = 0.0175$ μms^{-1}. Horizontal dimension: 140 μm. b) Hybrid patterns in three SCN-DC samples of different thicknesses. Top: δ = 30 μm; $V = 3V_0 = 0.0105$ μms^{-1}. Middle: δ = 60 μm; $V = 3V_0 = 0.0105$ μms^{-1}. Bottom (short-lived, localized pattern): δ = 140 μm; $V = 2V_0 = 0.007$ μms^{-1}. Horizontal dimension: 200 μm.

pled growth in the SCN-DC eutectic system. Inside the bistable domain, between the two limit velocities V_l and V_r, lamellar, rod-like and mixed patterns were observed depending on boundary conditions –mainly determined, in the present study, by the thickness δ of the sample– and the history of the experiment (hysteresis). For V below V_l, slowly relaxing labyrinth patterns (Figs. 3h and 3j) were observed in thicker samples (thus essentially free of confinement effects). Such patterns are typical of an isotropic, band-pattern forming system of large size. A rough estimate of V_l (between 0.0035 and 0.007 μms^{-1}) was obtained, but a more systematic experimental investigation at low velocities still remains challenging in practice. Confinement effects in intermediate-thickness samples permitted to stabilize well-defined 1D lamellar patterns. This also allowed us to establish that rod-like patterns are favored by smaller spacings and higher velocities, and lamellar patterns by larger spacings and lower velocities. Lamellar patterns exist over a larger range of spacings, extending to higher λ values than rod-like patterns. This seems, at first sight, roughly consistent with the λ_m scaling law, but the bistable character of the system still remains to be understood. In the following paragraphs, we initiate a discussion on fundamental aspects of the lamella-rod transition, on the basis of the above experimental results.

In the bistable range ($V_l < V < V_r$), the length of the lamellae was limited, in thick samples, by a propagative breakup instability [17, 19, 22]. The incipient Rayleigh-Plateau-like instability was however damped out, and lamellar breakup prevented, for lamellae in contact with a sample wall. Spatially extended, 1D periodic patterns made of lamellae connecting the two walls were thus stabilized over long times in confined-geometry samples. This allowed us to observe different instability modes that control the lamella-rod transition. Let us make the following two comments:

1- A zigzag instability [36] was observed during the first stages of the transients shown in Figs. 7 and 9. In their numerical study of the stability of lamellar patterns in model systems, Parisi and Plapp [16] found that the threshold λ_{zz} of the zigzag instability was ranging between $0.8\lambda_m$ and $1.2\lambda_m$, depending on alloy characteristics. The Λ data (lamellar patterns) reported in the graph of Fig. 4d are falling below 1.2 (except for a few $\Lambda > 1.2$ points corresponding to experiments

with a δ/λ ratio close to, or less than 1), which agrees well with that finding. Let us recall that the zigzag instability is of diffusive nature [10]. Above the threshold, there exists a finite interval of unstable wavevectors of the zigzag mode between 0 and an upper limit k_{zz} that increases when λ increases (and vanishes for $\lambda = \lambda_{zz}$). In other words, at given V, zigzag wavelengths larger than $L_{zz} = 2\pi/k_{zz}$ are unstable, while smaller ones do not amplify. Indeed, a decrease of the wavelength of stabilized chevron patterns when Λ increased was observed experimentally in Ref. [15]. Roughly speaking, in a confined-geometry system, a zigzag instability is expected to develop only if L_{zz} is (sufficiently) smaller than δ. This also means that, in practice, a zigzag instability will be observed if Λ is substantially larger than the nominal threshold for a bulk system. In Fig. 7, the λ distribution in the lamellar pattern at $V = 3V_0$ (before the velocity jump) was falling between $0.85\lambda_m$ and $1.0\lambda_m$ [36], therefore either in a stable, or slightly zigzag-unstable range –in the latter case, L_{zz} was much larger than δ, and the zigzag instability was hindered. In contrast, just after the velocity increase to $V = 6V_0$, Λ was ranging between 1.2 and 1.4. The lamellar pattern was then markedly unstable, at least in the large-λ region, and a zigzag instability with $L_{zz} < \delta$ amplified. In the present experiments, no stable chevrons patterns were observed: zigzag lamellae were unstable against breakup, and eventually transformed into rods.
2- In the late stage of the experiment shown in Fig. 7, straight lamellae with a smaller spacing underwent a delayed, but direct transformation into rods, without a transition via a zigzag instability. In that case, the incipient instability took the appearance of a 1λ mode [36]. According to Ref. [16], the threshold of the 1λ mode is larger than that of the zigzag instability. However, the wavelength of the 1λ mode, which is generally close to λ, was actually smaller than δ (while $L_{zz} > \delta$), in such a way that a 1λ instability could be observed in the confined system.

In more general terms, in an ordinary rod-like eutectic system, such as the SCN-DC alloy, lamellar patterns with relatively large spacings are stabilized as long as the characteristic wavelength(s) of active instability modes –which can be substantially larger than λ in the case of the zigzag instability– is (are) larger than the smallest size of the system, here, the sample thickness δ. The confinement effect operates as long as the Rayleigh-Plateau-like instability of the lamellae is damped out in contact with a sample wall. That instability determines the length of lamellae in a bulk system.

In thick SCN-DC samples, lamellar patterns were unstable at large solidification velocity ($V > V_r$), and rod-like patterns at low velocity ($V < V_l$), whatever the value of the spacing. In the bistable velocity domain, the Rayleigh-Plateau-like instability is propagative [22]. For a deeper insight, it would be a key to determine how the propagation rate of the instability depends on λ and V. A λ_m scaling seems unlikely, whereas it is relevant for most symmetry-breaking instabilities in coupled-growth patterns. There are several scaling lengths entering the eutectic-growth problem. In addition to the diffusion length $l_d = D/V$ (D: diffusion coefficient in the liquid), there are classically the thermal length $l_t = \Delta T_0/G$ (ΔT_0 being a temperature difference that characterizes the alloy), and the capillary length d_0, which is proportional to the surface tension γ of the solid-liquid interface. In a standard Jackson-Hunt (JH) approach [5], the α- and β-liquid interfaces (using a generic α and β notation for the two eutectic solid phases) are assumed to have the same average temperature. The effect of the temperature gradient is then negligible, and $\lambda_m \sim (d_0 l_d)^{1/2}$ is the sole relevant scaling length. However, in general, the α- and β-liquid interfaces are dissimilar, and their average temperatures within a lamella pair are not equal to each other. Then, instead of the averaged definition of l_t and d_0 as implicitly used above, it should be more accurate to consider the lengths l_t^ν and d_0^ν ($\nu = \alpha, \beta$) as defined for each solid phase. This can be made in a fully consistent JH approach, also called amended-JH analysis [42, 43]. As compared to the standard JH approach, that analysis reveals corrective terms

that depend on the ratio G/V –or the dimensionless parameter $\Gamma = l_d/l_t$. This, simply speaking, makes appear a direct dependence of the coupled-growth dynamics on V. As a first step toward a better understanding, it is tempting to emit the conjecture that the Rayleigh-Plateau-like instability of lamellar eutectic patterns is sensitive to the average temperatures T_ν of the two solid-liquid interfaces, or, rather, to the difference $\Delta T_{\alpha\beta} = T_\alpha - T_\beta$. In support to this hypothesis, it may be mentioned that (i) as it is well known, dissimilar volume phase fractions in the solid (η markedly different from 0.5) favor the formation of rods, and that (ii) numerical simulations considering a symmetric eutectic system with identical solid phases indicate that, at the eutectic point (equal volume phase fractions), rod-like patterns are not observed [17]. It is also worth mentioning that the so-called overstability effect that lowers the lamellar (and rod) elimination threshold on the small-spacing side was shown to depend on G/V [41]. This has been observed experimentally in several systems, including in thin SCN-DC samples [29], and found numerically in a model eutectic alloy with a symmetric phase diagram as well. The latter finding practically rules out a major contribution of $\Delta T_{\alpha\beta}$ in the overstability phenomenon. Our proposition is obviously not more than a tiny seed for further analysis. More work –essentially numerical simulations– would be needed before one being able to draw a definite Λ-V(-Γ) morphology diagram of lamellar and rod-like patterns in bulk SCN-DC samples.

Let us add a few important remarks. 1-It may be of strong relevance to consider the stability of elongated-rod patterns such as those found numerically in Refs. [17] and [21]. This remark refers to both the observation of short lamellae in mixed patterns, and the rod-to-lamellar transformation being mediated by the formation of elongated rods (Fig. 8). Incidentally, it seems that the rod-to-lamellar transformation (via rod elongation) is more continuous that the lamellar-to-rod one (via lamellar breakup) –except that, in practice, the rod-to-lamellar transformation also involves a nonlinear rod elimination process. This asymmetry may influence the hysteresis of the transition. 2-Interestingly, the highly nonlinear lamellar-rod-lamellar process of Fig. 9, which, again, presented a strongly propagative character, operated as a spacing adjustment mechanism to obtain a (more) uniform pattern. This phenomenon bears some similarities with the pattern smoothing process that has been shown experimentally and numerically to be associated with the propagation of a lamella elimination instability in thin samples [41]. There is, however, no evidence for a dynamic pattern selection mechanism in the strict sense of the term, in contrast to the phenomenology of the so-called tilt domains [11, 44]. 3-Finally, while periodic hybrid patterns such as those shown in Fig. 10b are unlikely to remain morphologically stable in bulk samples, they may form and persist over relatively long times as localized patches, thus contributing to the complex, slowly evolving spatio-temporal dynamics of mixed patterns.

5. Conclusion

Lamellar and rod-like eutectic patterns were observed in real time at low solidification velocity during directional solidification of the SCN-DC eutectic alloy in thin, thick, and confined-geometry samples. Morphology maps in terms of solidification velocity V, interphase spacing λ and sample thickness δ were plotted. These maps permit to locate the stability limits of rod-like and lamellar patterns in confined-geometry systems. The existence of a bistable domain of parameters was clearly evidenced (mixed patterns, hysteresis). Various secondary instability modes precursor to the lamellar breakup leading to the lamellar-to-rod transformation were revealed, as well as the rod elongation instability that governs the rod-to-lamellar transformation. Complex spatio-temporal phenomena involving labyrinth, oscillatory and hybrid patterns were

also reported, the multiscale dynamics of which is reminiscent of previous observations in directionally solidified eutectics [18, 19, 23, 45, 46]. The use of samples with various thicknesses was the experimental key to this analysis. Confinement effects during regular eutectic growth operate by preventing instability modes that control the relative stability of lamellar and rod-like patterns, and determine the spatio-temporal dynamics during coupled growth.

Clear light was shed on the dependence of the rod/lamellar dynamics on the interphase spacing and the solidification velocity. This led us to initiate a discussion on the possible effect of dissimilar physical parameters between the two solid phases, and their interfaces with the liquid, on the departure of the rod-*vs.*-lamellar stability from an ordinary $V^{-1/2}$ scaling.

It would be interesting to make a more quantitative analysis of the two-domain dynamics observed in Ref. [22] under the new light of the present study. More information is still needed before a general morphology diagram including the relevant ensemble of coupled-growth shapes can be defined. Additional experimental investigations in various eutectic alloys would be helpful for significant progress. Finally, the present experimental study should open the way to more systematic numerical simulations.

6. Acknowledgements

We thank Mathis Plapp for enlightening discussions. One of us (MS) benefited from a research grant of the French National Center for Space Studies (CNES), to which all the authors are grateful for long-term support to in-depth scientific research, focused on the Transparent Alloys program of the European Space Agency (ESA).

References

[1] W. Kurz, D. J. Fisher, Fundamentals of Solidification, Trans Tech Publications, Zurich, Switzerland (1998).
[2] J. A. Dantzig, M. Rappaz, Solidification, 2nd Edition, EPFL Press, Lausanne (2016).
[3] U. Hecht, L. Granasy, T. Pusztai, B. Boettger, M. Apel, V. Witusiewicz, L. Ratke, J. De Wilde, L. Froyen, D. Camel, B. Drevet, G. Faivre, S.G. Fries, B. Legendre, S. Rex, Multiphase solidification in multicomponent alloys, Mater. Sci. Eng. R. 46 (2004) 1-49.
[4] J. D. Hunt, K. A. Jackson, Binary Eutectic Solidification, Trans. Metall. Soc. AIME 236 (1966) 843-852.
[5] K. A. Jackson, J. D. Hunt, Lamellar and rod eutectic growth, Trans. Metall. Soc. AIME 236 (1966) 1129-1142.
[6] V. Fleury, J.-F. Gouyet, E. M. Leonetti, Branching in Nature, EDP Sciences, Springer (2001).
[7] S. Akamatsu, M. Plapp, Eutectic and peritectic solidification patterns, Current Opinion in Solid State and Materials Science 20 (2016) 46-54.
[8] M. Plapp, Three-dimensional phase-field simulations of directional solidification, J. Cryst. Growth 303 (2007) 49-57.
[9] M. Cross, P. Hohenberg, Pattern formation outside of equilibrium, Rev. of Mod. Phys. 65 (1993) 851-1112.
[10] P. Manneville, Dissipative structures and weak turbulence, Academic Press, Boston (1995).
[11] G. Faivre, J. Mergy, Tilt bifurcation and dynamical selection by tilt domains in thin-film lamellar eutectic growth: Experimental evidence of a tilt bifurcation, Phys. Rev. A 45 (1992) 7320-7329.
[12] G. Faivre, J. Mergy, Dynamic wavelength selection by tilt domains in thin-film lamellar eutectic growth, Phys. Rev. A 46 (1992) 963-972.
[13] A. Karma, A. Sarkissian, Morphological instabilities of lamellar eutectics, Met. Trans. A 27 (1996) 635-656.
[14] M. Ginibre, S. Akamatsu, G. Faivre, Experimental determination of the stability diagram of a lamellar eutectic growth front, Phys. Rev. E 56 (1997) 780-796.
[15] S. Akamatsu, S. Bottin-Rousseau, G. Faivre, Experimental evidence for a zigzag bifurcation in bulk lamellar eutectic growth, Phys. Rev. Lett. 93 (2004) 175701.
[16] A. Parisi, M. Plapp, Stability of lamellar eutectic growth, Acta Mater. 56 (2008) 1348-1357.
[17] A. Parisi, M. Plapp, Defects and multistability in eutectic solidification patterns, EPL 90 (2010) 26010.
[18] S. Liu, J. H. Lee, D. Enlow, R. Trivedi, Lamellar/rod transition in Al-Cu alloys, in Solidification Processes and Microstructures: A Symposium in Honor of Wilfried Kurz, Warrendale (2004) 257-262.

[19] S. Liu, J. H. Lee, R. Trivedi, Dynamic effects in the lamellar-rod eutectic transition, Acta Mater. 59 (2011) 3102-3115.
[20] M. Şerefoğlu, R. E. Napolitano, On the selection of rod-type eutectic morphologies: Geometrical constraint and array orientation, Acta Mater. 56 (2008) 3862-3873.
[21] M. Şerefoğlu, R. E. Napolitano, M. Plapp, Phase-field investigation of rod eutectic morphologies under geometrical confinement, Phys. Rev. E 84 (2011) 1539-3755.
[22] S. Bottin-Rousseau, V. T. Witusiewicz, U. Hecht, J. Fernandez, A. Laveron-Simavilla, S. Akamatsu, Coexistence of rod-like and lamellar eutectic growth patterns, Scripta Materialia 207 (2022) 114314.
[23] V. Trnovcova, P.P. Fedorov, C. Barta, V. Labas, V.A. Meleshina, B.P. Sobolev, Microstructure and physical properties of superionic eutectic composites of the LiF-RF3 (R = rare earth element) system, Solid State Ionics 119 (1999) 173-180.
[24] B. Yang, S. Li, X. Li, Y. Wang, H. Zhong, S. Feng, Microstructure and enhanced thermoelectric performance of Te-SnTe eutectic composites with self-assembled rod and lamellar morphology, Intermetallics 112 (2019) 106499.
[25] M. Şerefoğlu, S. Bottin-Rousseau, S. Akamatsu, G. Faivre, Dynamics of rod eutectic growth patterns in confined geometry, IOP Conference Series-Materials Science and Engineering 27 (2012) 012030.
[26] J. Eggers, E. Villermaux, Physics of liquid jets, Rep. Prog. Phys. 71 (2008) 036601.
[27] S. Bottin-Rousseau, M. Perrut, C. Picard, S. Akamatsu, G. Faivre, An experimental method for the in situ observation of eutectic growth patterns in bulk samples of transparent alloys, J. Cryst. Growth 306 (2007) 465-472.
[28] V.T. Witusiewicz, L. Sturz , U. Hecht, S. Rex, Thermodynamic description and unidirectional solidification of eutectic organic alloys: I. Succinonitrile-(D)camphor system, Acta Mater. 52 (2004) 4561-4571.
[29] S. Akamatsu, S. Bottin-Rousseau, M. Perrut, G. Faivre, L. Sturz, V. T. Witusiewicz, Real-time study of thin and bulk eutectic growth in Succinonitrile-(D)Camphor alloys, J. Cryst. Growth 299 (2007) 418-428.
[30] M. Perrut, S. Akamatsu, S. Bottin-Rousseau, G. Faivre, Long-time dynamics of the directional solidification of rodlike eutectics, Phys. Rev. E 79 (2009) 032602.
[31] M. Perrut, S. Bottin-Rousseau, G. Faivre, S. Akamatsu, Dynamic instabilities of rod-like eutectic growth patterns: A real-time study, Acta Mater. 61 (2013) 6802-6808.
[32] S. K. Aramanda, S. Khanna, S. K. Salapaka, K. Chattopadhyay, A. Choudhury, Crystallographic and Morphological Evidence of Solid-Solid Interfacial Energy Anisotropy in the Sn-Zn Eutectic System, Met. Mat. Trans. A 51 (2020) 6387-6405.
[33] S. Akamatsu, S. Bottin-Rousseau, G. Faivre, Determination of the Jackson–Hunt constants of the In-In_2Bi eutectic alloy based on in situ observation of its solidification dynamics, Acta Mater. 59 (2011) 7586-7591.
[34] E. J. Sullivan, J. A. Tomko, J.M. Skelton, J. M. Fitz-Gerald, P. E. Hopkins, J. A. Floro, Lamellar instabilities during scanning laser melting of Al–Cu eutectic and hypoeutectic thin films, Journal of Alloys and Compounds 865 (2021) 158800.
[35] S. Gurevich, A. Karma, M. Plapp, R. Trivedi, Phase-field study of three-dimensional steady-state growth shapes in directional solidification, Phys. Rev. E 81 (2010) 011603.
[36] Supplementary material is made available.
[37] L. Ratke, J. Alkemper, Ordering of the fibrous eutectic microstructure of Al-Al3Ni due to accelerated solidification conditions, Acta Mater. 48 (2000) 1939-1948.
[38] D. A. Pawlak, K. Kolodziejak, S. Turczynski, J. Kisielewski, K. Rozniatowski, R. Diduszko, M. Kaczkan, M. Malinowski, Self-organized, rodlike, micrometer-scale microstructure of Tb3Sc2Al3O12-TbSCO3 : Pr eutectic, Chemistry of Materials 18 (2006) 2450-2457.
[39] H. Walker, S. Liu, J. H. Lee, R. Trivedi, Eutectic growth in three dimensions, Met. Mat. Trans. A 38A (2007) 1417-1425.
[40] L. Wei, Z. Zhao, J. Gao, K. Cui, J. Guo, S. Chen, L. Liu, Morphological instability of lamellar structures in directionally solidified Ni-Ni3Si alloys, J. Cryst. Growth 483 (2018) 275-280.
[41] S. Akamatsu, M. Plapp, G. Faivre, A. Karma, Overstability of lamellar eutectic growth below the minimum-undercooling spacing, Metal. Mater. Trans. A 35 (2004) 1815-1828.
[42] K. Brattkus, B. Caroli, C. Caroli, B. Roulet, Lamellar eutectic growth at large thermal-gradient.1. Stationary patterns, J. Physique 51 (1990) 1847-1864.
[43] J. Mergy, G. Faivre, C. Guthmann, R. Mellet, Quantitative-determination of the physical parameters relevant to the thin-film directional solidification of the CBr4-C2Cl6 eutectic alloy, J. Cryst. Growth 134 (1993) 353-368.
[44] P. Coullet, R. E. Goldstein, G. H. Gunaratne, Parity-breaking transitions of modulated patterns in hydrodynamic systems, Phys. Rev. Lett. 63 (1989) 1954.
[45] M. Neuroth, K. Recker, F. Wallrafen, Investigations on the directional solidification of the eutectic LiF-LiBaF3, Zeitschrift für Kristallographie 209 (1993) 295-302.
[46] M. Kellner, W. Kunz, P. Steinmetz, J. Hoetzer, B. Nestler, Phase-field study of dynamic velocity variations during directional solidification of eutectic NiAl-34Cr, Comput. Mater. Sci. 145 (2018) 291–305

Appendix A.

Symbol	Definition	Unit
C_E	Eutectic concentration	mol%
d_0	Capillary length	μm
D	Solute diffusion coefficient in the liquid	$\mu m^2 s^{-1}$
G	Temperature gradient	Kcm^{-1}
l_t	Thermal length	μm
t	Time	s
T_E	Eutectic temperature	K (or ^oC)
V	Pulling velocity	μms^{-1}
x, y, z	Space variables	μm
δ	Sample thickness	μm
T_ν	Average temperature of the ν-liquid interface	K
η	Volume phase fraction of the DC phase β in the solid	–
Γ	Ratio l_d/l_t	–
λ	Interphase spacing	μm
λ_m	Minimum-undercooling spacing	μm
λ_{el}	Rod elimination threshold	μm
λ_{sp}	Rod splitting threshold	μm
λ_{zz}	Zigzag instability threshold	μm
Λ	Dimensionless interphase spacing λ/λ_m	–
$\nu = \alpha; \beta$	Solid phases	–

Table A1: Physical variables and parameters